

# The Different Dynamic Influences of Typhoon Kalmaegi on two Pre-existing Anticyclonic Ocean Eddies

Yihao He<sup>1</sup>, Xiayan Lin<sup>1,2,\*</sup>, Guoqing Han<sup>1</sup>, Yu Liu<sup>1,3</sup> and Han Zhang<sup>2,3,\*</sup>

<sup>1</sup> Marine Science and Technology College, Zhejiang Ocean University, Zhoushan 316022, China;

<sup>2</sup> State Key Laboratory of Satellite Ocean Environment Dynamics, Second Institute of Oceanography, Ministry of Natural Resources, Hangzhou 310012, China;

<sup>3</sup> Southern Marine Science and Engineering Guangdong Laboratory (Zhuhai), Zhuhai 519082, China

\*Correspondence: Xiayan Lin (linxiayan@zjou.edu.cn) and Han Zhang (zhanghan@sio.org.cn)

**Abstract:** Using multi-source observational data and GLORYS12V1 reanalysis data, we conduct a comparative analysis of different responses of two warm eddies, AE1 and AE2 in the northern South China Sea to Typhoon Kalmaegi during September 2014. The findings of our research are as follows: (1) For horizontal distribution, the area and the sea surface temperature (SST) of AE1 and AE2 decrease by about 31% (36%) and 0.4 °C (0.6 °C). The amplitude, Rossby number ( $R_o$ =relative vorticity/Coriolis parameter) and eddy kinetic energy (EKE) of AE1 increases by 1.3 cm (5.7%),  $1.4 \times 10^{-2}$  (20.6%) and  $107.2 \text{ cm}^2 \text{ s}^{-2}$  (49.2%) after the typhoon, respectively, while AE2 weakens and the amplitude, Rossby number and EKE decreased by 3.1 cm (14.6%),  $1.6 \times 10^{-2}$  (26.2%) and  $38.5 \text{ cm}^2 \text{ s}^{-2}$  (20.2%), respectively. (2) In vertical direction, AE1 demonstrates enhanced convergence, leading to an increase in temperature and a decrease in salinity above 150 m. The response below the mixing layer depth (MLD) is particularly prominent (1.3 °C). In contrast, AE2 experiences cooling and a decrease in salinity above the MLD. Below the MLD, it exhibits a subsurface temperature drop and salinity increase due to the upwelling of cold water induced by the suction effect of the typhoon. (3) The disparity in the responses of the two warm eddies can be attributed to their different positions relative to Typhoon Kalmaegi. Warm eddy AE1, with its center to the left of the typhoon's path, experiences a positive work effect as the typhoon passes by. The negative wind stress curl in AE1 triggers a negative Ekman pumping velocity (EPV), further enhancing the converging sinking of the upper warm water, thereby strengthening AE1. On the other hand, warm eddy AE2, situated closer to the center of the typhoon, weakens due to the cold suction caused by the strong positive wind stress curl in the typhoon's center. Same polarity eddies may have different response to typhoons. The distance between eddies and typhoons, eddies intensity and the background field need to be considered.

删除了:  $\text{cm}^2$

删除了:  $\text{cm}^2$

删除了: locates on

删除了:

删除了: side

删除了: (?) by

删除了:

删除了: situates

删除了: ,

删除了: t

41 **1. Introduction**

42 Tropical cyclones (TCs), as they traverse the vast ocean, interact with oceanic mesoscale processes,  
43 particularly with mesoscale eddies, representing a crucial aspect of air-sea interaction (Shay and Jaimes,  
44 2010; Lu et al., 2016; Song et al., 2018; Ning et al., 2019; Sun et al., 2023). The South China Sea (SCS)  
45 experiences an average of six TCs passing through each year (Wang et al., 2007), causing prominent  
46 exchange of energy and mass between air and sea (Price, 1981). Meanwhile, due to the influence of the  
47 Asian monsoon, intrusion of the Kuroshio Current, and complex topography, the Northern South China  
48 Sea (NSCS) also encounters frequent eddy activities (Xiu et al., 2010; Chen et al., 2011). These  
49 mesoscale oceanic eddies often play significant roles in mass and heat transport and air-sea interaction.  
50 This unique setting offers an exceptional opportunity to investigate the generation, evolution, and  
51 termination of mesoscale eddies and their interaction with TCs.

52 Pre-existing mesoscale eddies play a crucial role in the feedback mechanism between the ocean and  
53 TCs. Cyclonic eddies (cold eddies) enhance the sea surface cooling effect under TCs conditions, resulting  
54 in TCs weakening, due to their thermodynamic structures and cold-water entrainment processes that  
55 reduce the heat transfer from the sea surface to the TCs through air-sea interaction (Ma et al., 2017; Yu  
56 et al., 2021). In contrast, anticyclonic eddies (warm eddies) suppress this cooling effect, leading to TCs  
57 intensification (Shay et al., 2000; Walker et al., 2005; Lin et al., 2011; Wang et al., 2018). Warm eddies  
58 have a thicker upper mixed layer, which stores more heat. When a TC passes over a warm eddy, it  
59 increases sensible heat and water vapor in TC's center, which are closely related to the TC's  
60 intensification (Wada and Usui, 2010; Huang et al., 2022). Furthermore, the downwelling within warm  
61 eddies hinders the upwelling of cold water, reducing the apparent sea surface cooling caused by the TCs.  
62 These processes weaken the oceanic negative feedback effect and help to sustain or even strengthen TC's  
63 development. TCs cause the strengthening of cyclonic eddies, leading to positive potential vorticity  
64 anomalies (Zhang et al., 2020).

65 On the other hand, TCs also have a notable impact on the intensity, size, and movement of mesoscale  
66 eddies. In general, TCs strengthen cold eddies and can even lead to the formation of new cyclonic eddies  
67 in certain situations (Sun et al., 2014), while TCs accelerate the dissipation of anticyclonic eddies (Zhang  
68 et al., 2020). The strengthening effect of TCs on cold eddies is related to the positions between cold  
69 eddies and TCs, the intensity of eddies, and TC-induced geostrophic response (Lu et al., 2016; Yu et al.,

删除了:

删除了: interface

删除了: ation

删除了: On one hand, from a thermodynamic perspective, TCs derive their development and sustenance energy from the ocean.

删除了: through

删除了: While from a dynamic perspective,

删除了:

删除了: , then accelerates the currents and exacerbates global warming, ultimately further promotes TCs enhancement

80 2019; Lu et al., 2023). Cyclonic eddies on the left side of the TC's track were more intensely affected by  
81 the TC, and eddies with shorter lifespans or smaller radii are more susceptible to the influence of TCs.  
82 The dynamic adjustment process of eddy and the upwelling induced by TC itself leads to changes in the  
83 three-dimensional structure of the cyclonic eddies, including ellipse deformation and re-  
84 axisymmetrization on the horizontal plane, resulting in eddy intensification. The presence of cold eddies  
85 not only exacerbates the sea surface cooling in the post-TC cold eddy region but also accompanies a  
86 decrease in sea level anomaly (SLA), deepening of the mixed layer, a strong cooling in the subsurface,  
87 increased chlorophyll-a concentration within the eddy, and substantial increases in EKE and available  
88 potential energy (Shang et al., 2015; Liu and Tang, 2018; Li et al., 2021; Ma et al., 2021).

删除了: typhoon

删除了: typhoon

删除了: typhoon

89 Generally, TCs lead to a reduction of warm eddies, while the sea surface cooling is not significant,  
90 typically within 1°C. However, there is a noticeable cooling and increased salinity in the subsurface layer,  
91 accompanied by an upward shift of the 20°C isotherm, a decrease in heat and kinetic energy (Lin et al.,  
92 2005; Liu et al., 2017; Huang and Wang, 2022). Lu et al. (2020) propose that TCs primarily generate  
93 potential vorticity input through the geostrophic response. When a TC passes over an eddy, there is a  
94 significant positive wind stress curl within the TC's maximum wind radius, which induces upwelling in  
95 the mixed layer due to the divergence of the wind-driven flow field. This upward flow compresses the  
96 thickness of the isopycnal layers below the mixed layer, resulting in a positive potential vorticity anomaly.  
97 By analyzing the time series of ocean kinetic energy, available potential energy (APE), vorticity budget,  
98 and potential vorticity (PV) budget, Rudzin and Chen (2022) find that the positive vertical vorticity  
99 advection caused the TC to eliminate the warm eddy from bottom to top after passing through. Under

删除了: typhoons

删除了: typhoons

删除了: typhoon

删除了: typhoon's

100 the interaction of the strong TC wind stress in the eye area of the TC and the subsurface ocean current  
101 field, the early-onset of a near-inertial wake caused the disappearance of the warm eddy. However, the  
102 projection of TC wind stress onto the eddy and the relative position of the warm eddy to the TC can lead  
103 to different responses. According to the classical description of TC-induced upwelling, strong upwelling  
104 occurs within twice the maximum wind radius of the TC center, while weak subsidence exists in the vast  
105 area outside the upwelling region (Price, 1981; Jullien et al., 2012). The warm eddy located directly  
106 beneath the TC's path weakens due to the cold suction caused by the TC's center. However, for warm  
107 eddies located beyond twice the maximum wind radius, they are influenced by the TC's wind stress curl  
108 and the downwelling within the eddy itself, resulting in the convergence of warm water in the upper

删除了: typhoon

删除了: typhoon

删除了: typhoon

删除了: locates

删除了: typhoon's

删除了: typhoon's

删除了: locate

删除了: typhoon's

124 layers of the eddy, an increase in mixed layer thickness, and an increase in heat content, leading to a  
125 warming response to the [TC](#) (Jaimes and Shay, 2015).

126 The NSCS encounters high frequency and intense [TCs](#), concurrently, there is notable activity of  
127 mesoscale eddies in this region. Based on in-situ datasets, multi-platform satellite measurements, and  
128 GLORYS12V1 reanalysis data, we investigate [how the upper ocean in](#) two anticyclonic eddies [responds](#)  
129 to Typhoon Kalmaegi. This marks the initial effort to characterize the different physical variations  
130 induced by TCs within two same polarity eddies, contributing to a better understanding [of](#) the role played  
131 by mesoscale eddies in modulating interactions between TCs and the ocean. Section 2 provides an  
132 overview of the data and methods utilized in this research. Section 3 analyzes the physical parameters of  
133 warm eddies, vertical temperature and salinity variations, and explores the different responses of warm  
134 eddies both inside and outside the typhoon affected region. Section 4 offers a comprehensive discussion  
135 and Section 5 gives a summary.

## 136 2. Data and Methods

### 137 2.1. Data

138 The six-hourly best-track typhoon datasets are obtained from the Joint Typhoon Warning Center  
139 (JTWC, <http://www.usno.navy.mil/JTWC>, last access: 3 February, 2021), the Japan Meteorological  
140 Agency (JMA, <https://www.jma.go.jp/jma/jma-eng/jma-center/rsmc-hp-pub-eg/besttrack.html>, last  
141 access: 3 February, 2021), and the China Meteorological Administration (CMA,  
142 <http://tcdata.typhoon.gov.cn>, last access: 3 February, 2022). The data contain the TCs' center locations,  
143 the minimum central pressure, maximum sustained wind speed, and intensity category. The translation  
144 speed of typhoons is calculated by dividing the distance travelled by each typhoon within a 6-hour  
145 interval by the corresponding time. In this paper, Typhoon Kalmaegi and tropical storm Fung-wong are  
146 studied (Fig. 1).

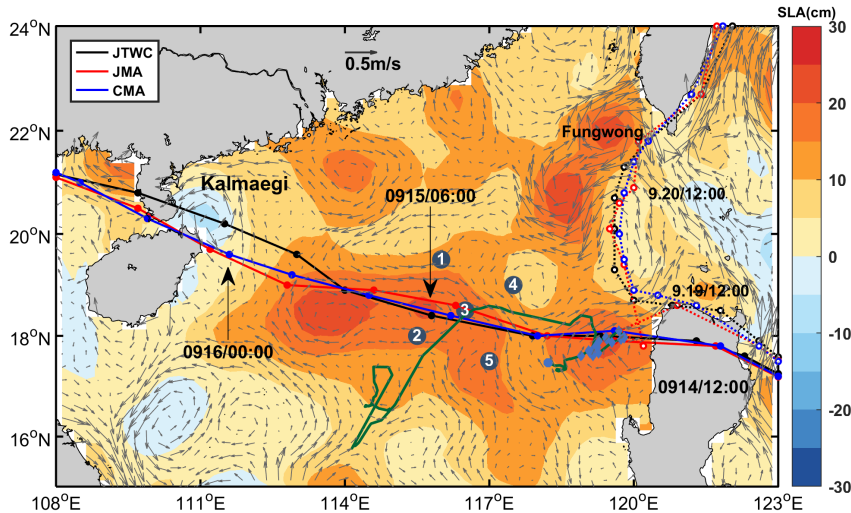
删除了: typhoon

删除了: tropical cyclones (

删除了: )

删除了: on upper ocean responses





151  
 152 **Figure 1.** The tracks of Typhoon Kalmaegi (solid lines with dots) and tropical storm Fung-wong (dashed lines with  
 153 hollow dots) as provide by the Joint Typhoon Warning Center (JTWC, black), Japan Meteorological Agency (JMA,  
 154 red), and China Meteorological Administration (CMA, blue). The colour shading represents the sea surface level  
 155 anomaly on 13 September, 2014, while the gray arrows illustrate the geostrophic flow field. The numbered blue dots  
 156 represent the positions of the five buoy/mooring stations, the green line illustrates the trajectory of Argo 2901469,  
 157 and the blue diamond's mark the positions of Argo 2901469 inside the eddy AE2 from 26 August 2014 to 25 October  
 158 25, 2014.

159 The daily Sea Level Anomaly (SLA) and geostrophic current data [are provided](#) by Archiving,  
 160 Validation, and Interpretation of Satellite Data in Oceanography (AVISO) product (CEEMS,  
 161 <https://marine.copernicus.eu/>, last access: 14 [February](#), 2022). This dataset combines satellite data from  
 162 Jason-3, Sentinel-3A, HY-2A, Saral/AltiKa, Cryosat-2, Jason-2, Jason-1, T/P, ENVISAT, GFO, and  
 163 ERS1/2. The spatial resolution of the product is  $1/4^\circ \times 1/4^\circ$ . The period from 1 September to 30  
 164 September 2014 was used.

165 The daily Sea Surface Temperature (SST) data used in this study is derived from the Advanced Very  
 166 High-Resolution Radiometer (AVHRR) product data provided by the National Oceanic and Atmospheric  
 167 Administration (NOAA). The data is obtained from the Physical Oceanography Distributed Active  
 168 Archive Center (PODAAC) at the NASA Jet Propulsion Laboratory (JPL)  
 169 ([ftp://podaac.jpl.nasa.gov/documents/dataset\\_docs/avhrr\\_pathfinder\\_sst.html](ftp://podaac.jpl.nasa.gov/documents/dataset_docs/avhrr_pathfinder_sst.html), last access: 16 March,  
 170 2022). The spatial resolution of the data is  $1/4^\circ \times 1/4^\circ$ .

171 Argo data, including profiles of temperature and salinity from surface to 2000 m depth are obtained  
 172 from the real-time quality-controlled Argo data base (Euro-Argo, <https://dataselection.euro-argo.eu/>, last  
 173 access: 4 April, 2022). We select Argo float number 2901469, situated in an anticyclonic eddy and in  
 174 close proximity to [Typhoon](#) Kalmaegi, both before and after the typhoon's passage in 2014. Profiles of  
 175 this Argo are also used to validate the vertical distribution of temperature and salinity from  
 176 GLORYS12V1.

删除了: Febururay

删除了: ,

删除了: t

删除了: ocean

删除了: typhoon

182 For this study, we also utilize in-situ data from a cross-shaped array consisting of five stations,  
183 comprising five moored buoys and four subsurface moorings (refer to Fig. 1). More specific information  
184 can be found in Zhang et al. (2016). To investigate the impact of the typhoon on a warm eddy, we select  
185 the temperature and salinity data from Station 5, situated to the left of Kalmaegi's track.

186 The wind speed data is sourced from the European Centre for Medium-Range Weather Forecasts  
187 (ECMWF) ERA-Interim reanalysis assimilation dataset ([https://apps.ecmwf.int/datasets/data/interim-  
188 full-daily/levtype=sfc/](https://apps.ecmwf.int/datasets/data/interim-full-daily/levtype=sfc/), last access: 5 January, 2023). We used the reanalysis data of surface winds at a  
189 height of 10 meters above sea level for TCs. The selected data has a spatial resolution of  $1/4^\circ \times 1/4^\circ$  and  
190 a temporal resolution of 6 hours, with four updates per day (00:00, 06:00, 12:00, and 18:00 UTC). The  
191 data corresponds to September 2014.

192 The Global Ocean Reanalysis Product GLOBAL MULTIYEAR\_PHY\_001\_030 (GLORYS12V1),  
193 provides by the Copernicus Marine Environment Monitoring Service (CMEMS,  
194 <https://marine.copernicus.eu/>, last access: 23 March, 2022) is used in this study too. This reanalysis  
195 product utilized the NEMO 3.1 numerical model coupled with the LIM2 sea ice model, and forced with  
196 ERA-Interim atmospheric data. The model assimilated along-track altimeter data from satellite  
197 observations (Pujol et al., 2016), satellite sea surface temperature data from AVHRR, sea ice  
198 concentration from CERSAT (Ezraty et al., 2007), and vertical profiles of temperature and salinity from  
199 the CORAv4.1 database (Cabanes et al., 2012). The temperature and salinity biases were corrected using  
200 a 3D-VAR scheme. The horizontal resolution is  $1/12^\circ \times 1/12^\circ$ , and it has 50 vertical levels. The  
201 temperature and salinity from 1 September to 30 September 2014 were chosen.

202 GLORYS12V1 is a widely used and applicable dataset, to evaluate its temperature profiles, the Argo  
203 profiles and in-situ data of Station 5 were compared (Fig. 2). The GLORYS12V1 data exhibit good  
204 agreement with Argo profiling floats, the maximum difference between them is less than  $0.2^\circ\text{C}$ , the Root  
205 Mean Square (RMS) is 0.02. However, there are some discrepancies between the GLORYS12V1 and  
206 the Station 5 data, with the largest difference occurring at the depths of 30 m (mixed layer) and 78 m  
207 (thermocline), both differing by  $0.6^\circ\text{C}$ , while below 150 m, the difference is quite small. The RMS is  
208 0.09. The RMS between GLORYS12V1 and Station 2 (Station 4) is 0.14 (0.10) (Figures not shown).

209 Because the GLORYS12V1 assimilates Argo data and the vertical resolution of Argo profile above 100m  
210 is 5 m, but the vertical interval of buoy array is 20 m. Therefore, the large deviations exist at mixed layer  
211 and thermocline during the typhoon in in-situ data of Station 5. Overall, GLORYS12V1 reproduces the  
212 observed ocean temperature accurately, it is reasonable to use it to investigate the vertical response of  
213 anticyclonic eddies to Typhoon Kalmaegi.

删除了: situates

删除了: along

删除了: track of

删除了: This dataset is widely used for weather analysis and numerical forecasting. The wind field data used in this study primarily focuses

删除了: on

删除了: utilize

删除了: REA- NALYSIS

设置了格式: 非突出显示

删除了: form

删除了: to study

删除了: with

删除了:

设置了格式: 非突出显示

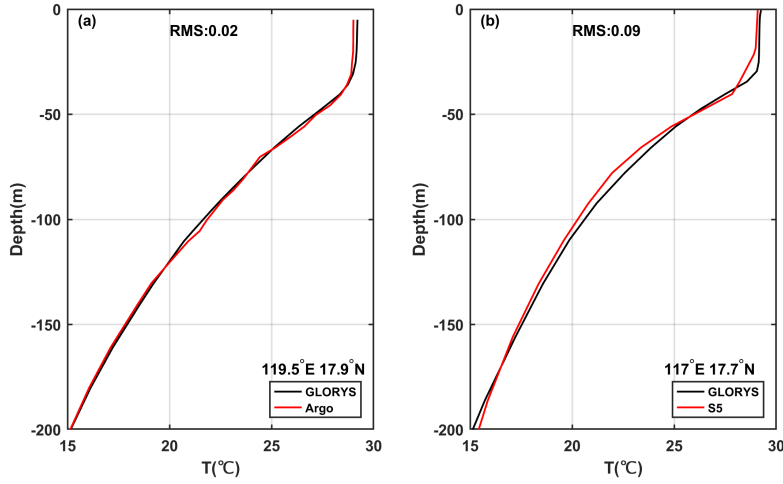
设置了格式: 非突出显示

删除了: upper 100 m in Argo profile

删除了: [RE-WRITE]

删除了: by

删除了: typhoon



231  
 232 **Figure 2.** Evaluation of GLORYS12V1 data performance during September 2014. (a) Vertical monthly mean  
 233 temperature within the anticyclonic eddy AE2 (119.5°E 17.9°N) as measured by Argo float 2901469. (b)  
 234 Comparison of vertical monthly mean temperature recorded at Station 5 (117°E 17.7°N).

235 **2.2. Methods**

236 Vorticity is a vector that characterizes the local rotation within a fluid flow. Mathematically, it is  
 237 defined as the curl of the velocity vector. In most cases, when referring to vorticity, it specifically pertains  
 238 to the vertical component of the vorticity. It is calculated from:

239 
$$\zeta = \frac{\partial v}{\partial x} - \frac{\partial u}{\partial y} . \quad (1)$$

240  $u$  and  $v$  are the zonal (eastward) and meridional (northward) geostrophic velocities, respectively. They  
 241 are derived from altimeter sea level anomaly data ( $\eta$ ):

242 
$$u = -\frac{g}{f} \frac{\partial \eta}{\partial y} , v = \frac{g}{f} \frac{\partial \eta}{\partial x} . \quad (2)$$

243 Here,  $g$  is the acceleration of gravity,  $f$  is the Coriolis frequency. Vorticity is considered a  
 244 fundamental characteristic of mesoscale eddies, positive vorticity signifies cyclonic eddies, while  
 245 negative vorticity indicates anticyclonic eddies.

246 The Rossby number ( $Ro$ ) is a dimensionless number describing fluid motion, and it is the ratio of  
 247 relative vorticity to planetary vorticity, reflecting the relative importance of local non-geostrophic motion  
 248 versus large-scale geostrophic motion. The larger the Rossby number, the stronger the local non-  
 249 geostrophic effect, and the definition of this parameter is:

250 
$$Ro = \frac{\zeta}{f} . \quad (3)$$

删除了: to

252 Eddy Kinetic Energy (EKE) is a measure of the energy associated with mesoscale eddies, which  
 253 indicates the intensity of eddies. It is typically calculated using the anomalies of the geostrophic velocity:

$$254 \quad EKE = \frac{1}{2}(u'^2 + v'^2) , \quad (4)$$

255 where  $u'$  represents the anomaly of the geostrophic zonal (eastward) velocity,  $v'$  represents the anomaly  
 256 of the meridional (northward) velocity.

257 To evaluate the impact of a typhoon on an anticyclonic eddy, the calculation begins with determining  
 258 the wind stress:

$$259 \quad \tau = \rho_a C_d U_{10} \overline{U_{10}} , \quad (5)$$

260 where  $\rho_a$  is the air density, assumed to be a constant value of  $1.293 \text{ kg m}^{-3}$ ,  $U_{10}$  represents the 10-  
 261 meter wind speed. And  $C_d$  is the drag coefficient at the sea surface (Oey et al., 2006):

$$262 \quad C_d \times 1000 = \begin{cases} 1.2 & U_{10} \leq 10 \text{ m s}^{-1} \\ 0.49 + 0.65 U_{10} & 11 \leq U_{10} < 19 \text{ m s}^{-1} \\ 1.364 + 0.234 U_{10} - 0.00023158 U_{10}^2 & 19 \leq U_{10} \leq 100 \text{ m s}^{-1} \end{cases} . \quad (6)$$

263 The wind stress curl is calculated by (Kessler, 2006):

$$264 \quad \text{curl}(\tau) = \frac{\partial \tau_y}{\partial x} - \frac{\partial \tau_x}{\partial y} , \quad (7)$$

265 where  $\tau_x$  and  $\tau_y$  are the eastward and northward wind stress vector components, respectively. The curl  
 266 represents the rotation experienced by a vertical air column in response to spatial variations in the wind  
 267 field.

268 The Ekman pumping velocity (EPV) represents the ocean upwelling rate, which can be used to study  
 269 the contribution of typhoons to regional ocean upwelling. Positive means upwelling, negative represents  
 270 downwelling:

$$271 \quad EPV = \text{curl}\left(\frac{\tau}{\rho f}\right) , \quad (8)$$

272 where the wind stress is obtained from Eq. (7),  $\rho$  is seawater density, the value is  $1025 \text{ kg m}^{-3}$ , and  $f$   
 273 is the Coriolis frequency.

274 The buoyancy frequency is a measure of the degree to which water is mixed and stratified. In a stable  
 275 temperature stratification, the fluid particles move in the vertical direction after being disturbed, and the  
 276 combined action of gravity and buoyancy always makes them return to the equilibrium position and  
 277 oscillate due to inertia. When  $N^2 < 0$ , the water is in an unstable state:

$$278 \quad N^2 = -\frac{g}{\rho} \frac{\partial \rho}{\partial z} \quad (9)$$

279 where  $\rho$  is seawater density,  $g$  is the acceleration of gravity, and  $z$  is the depth.

280 **3. Results**

281 **3.1. Typhoon and pre-existing eddies in the NSCS**

282 **3.1.1. Track of Typhoon Kalmaegi and tropical storm Fung-wong**

283 Typhoon Kalmaegi strengthens into a typhoon by 1200 UTC on 13 September and emerged over the  
284 warm waters of the Northern South China Sea (NSCS) by 1500 UTC on 14 September, with maximum  
285 sustained winds of  $33 \text{ m s}^{-1}$  (Fig. 3-4). During this period, the NSCS experiences predominantly weak  
286 vertical wind shear and is characterized by multiple anticyclonic warm eddies (Fig. 3). Subsequently,  
287 Typhoon Kalmaegi undergoes two rapid intensification phases between 15 and 16 September. The first  
288 intensification occurs at 0000 UTC on 15 September, propelling Kalmaegi to category 1 status with  
289 surface winds surpassing  $35 \text{ m s}^{-1}$ . By 1200 UTC on 15 September, Kalmaegi experiences a second, even  
290 more rapid intensification, with winds reaching  $40 \text{ m s}^{-1}$  in less than 12 hours. Throughout this  
291 intensification stage, Kalmaegi encounters two warm eddies: anticyclonic eddy AE1, is positioned to the  
292 left of the typhoon's path, with its core situated on the periphery of the typhoon's two-times maximum  
293 wind radius (Fig.3c-d), AE1 has a lifespan of 105 days from 26 June to 8 October and is positioned at  
294  $17^{\circ}\text{N}$ - $20^{\circ}\text{N}$ ,  $113^{\circ}\text{E}$ - $116^{\circ}\text{E}$ . AE2 precisely intersects with the typhoon's trajectory, and its core nearly  
295 coincides with the maximum wind radius of the typhoon (Fig.3b-d). It has a lifespan of 89 days from 24  
296 August to 20 November and is located at  $17^{\circ}\text{N}$  - $19^{\circ}\text{N}$ ,  $118^{\circ}\text{E}$  - $120^{\circ}\text{E}$ . Kalmaegi makes landfall on Hainan  
297 Island at 0300 UTC on 16 September, with a minimum central pressure of 960 hPa and a maximum wind  
298 speed of  $40 \text{ m s}^{-1}$ . After landfall, Typhoon Kalmaegi gradually weakens and dissipates. During its  
299 crossing of the NSCS, the five mooring stations are affected. Stations 1 and 4 are on the right side of  
300 Typhoon Kalmaegi's track, while Stations 2 and 5 are on the left side. Unfortunately, the wire rope of the  
301 buoy at Station 3 is destroyed by Kalmaegi, resulting in missing data from 15 September. Among the  
302 stations, Station 5 is on the left of typhoon track and outside AE2, so its data is used in our study.

303 Tropical storm Fung-wong initially moves quickly in a northwest direction after formation. On 19  
304 September, it enters the Luzon Strait and decelerates. It makes landfall in Taiwan on the 21 September  
305 and subsequently lands in Zhejiang on the 22 September before gradually dissipating. When crossing the  
306 Luzon Strait at 1200 UTC on 19 September, anticyclonic eddy AE2 is on the left side of Fung-wong,  
307 with a distance of just over 100 km from its center.

删除了: m

删除了: m

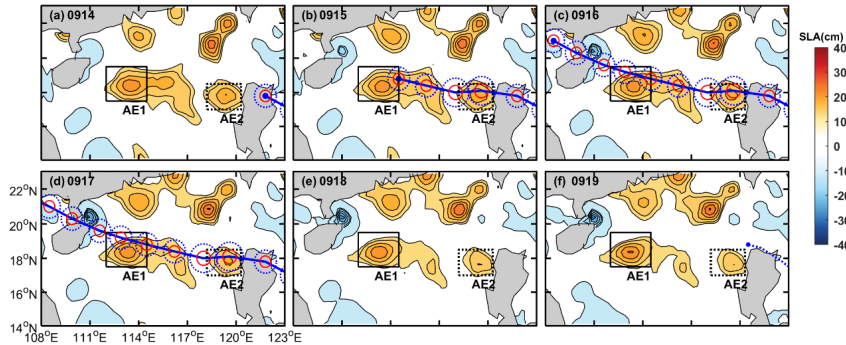
删除了: situates

删除了: Throughout this intensification stage, Kalmaegi encounters two warm eddies: anticyclonic eddy AE1, locates to the left of the typhoon's path, its core situates on the periphery of two times maximum wind radius of typhoon (Fig.3c-d)

删除了: ing

删除了: AE2, precisely intersecting with the typhoon's trajectory, its core almost coincident with maximum wind radius of typhoon (Fig.3b-d)....

删除了: .



320  
321 **Figure 3.** The variations in sea level anomaly before and after Typhoon Kalmaegi moved over the anticyclonic eddies  
322 AE1 and AE2 between 14 September and 19 September (a-f). The black solid rectangle represents the area of AE1,  
323 while the black dashed rectangle represents the area of AE2. The blue solid line depicts the path of Typhoon  
324 Kalmaegi, the solid red and dashed blue circles are the one- and two-times maximum wind radius of the typhoon,  
325 while the blue dotted line in (f) is the path of tropical storm Fung-wong (best-track data sourced from CMA).

### 326 3.1.2. Eddy characteristics distribution

327 Satellite SLA measurements have proven to be highly effective and widely used for identifying and  
328 quantifying the intensity of ocean eddies (Li et al., 2014). In Fig. 3, two warm eddies with clear positive  
329 ( $> 13$  cm) SLA are observed along the Typhoon Kalmaegi's track. During the period of 15 to 16  
330 September, the typhoon passes over two warm anticyclonic eddies, AE1 and AE2. Before the typhoon,  
331 AE1 is the most prominent eddy in the SCS, with an amplitude of 23.0 cm, and a radius of 115.5 km.  
332 AE2, located west of Luzon Island, has an amplitude of 21.2 cm, with a radius of approximately 65.5  
333 km. Tracing back to 2 months (figure is not shown), AE1 propagates slowly westward with about  $0.1 \mu\text{m}$   
334  $\text{s}^{-1}$ , while AE2 is generated on 24 August. During 14 to 19 September, the amplitude of AE1 increases  
335 1.3 cm. The area of the AE1 decreases by approximately 31% from  $1.3 \times 10^5 \text{ km}^2$  to  $9.1 \times 10^4 \text{ km}^2$  and  
336 splits into two eddies. When Typhoon Kalmaegi crosses the core of AE2 at 1500 UTC on 14 September,  
337 and tropical storm Fung-wong moves over the northeast of AE2 at 1200 UTC on 19 September, the  
338 amplitude decreases by 3.1 cm. The area of the AE2 decreases by approximately 36% from  $4.2 \times 10^4 \text{ km}^2$   
339 to  $2.7 \times 10^4 \text{ km}^2$ .

340 Because of intense solar radiation in September, the SST in the SCS is generally above  $28.5^\circ\text{C}$  prior  
341 to the arrival of Typhoon Kalmaegi (Fig. 4a). As a fast-moving typhoon with a mean moving speed of  
342 over  $8 \text{ m} \cdot \text{s}^{-1}$ , Kalmaegi induces a larger cooling area and intensity on the right side of its path compared  
343 to the left side (Price, 1981). During the passage of Kalmaegi, the lowest SST on the right side of typhoon  
344 decreases to  $27.2^\circ\text{C}$ . Even after the typhoon has passed, a cold wake could still be observed on the right  
345 side of its path, persisting for over a week (Fig. 4c).

346 The pre-existing warm eddy AE1 begins to cool down before Kalmaegi reached the NSCS, dropping  
347 to  $28.4^\circ\text{C}$  on 14 September. During this period, the mean SST within AE1 increases slightly to  $28.6^\circ\text{C}$   
348 (Fig. 5a). However, as cooler water from the right side of the typhoon track is subsequently advected into

删除了: typhoon

删除了: typhoon

删除了: locates

删除了: exhibites

删除了: m

删除了: .

删除了: Mesoscale eddies, due to their special thermodynamic structure and varying positions in relation to the TC, can modulate distinct sea surface temperature changes and exhibit different characteristics.

359 the AE1 region (Fig. 4c), the SST decreases and reaches 28.0 °C on September 19, which is 0.4°C lower  
360 than that before the typhoon. The average SST drop in AE2 is evident, with SST starting to decline before  
361 14 September and reaching its lowest temperature (28.1°C) on 15 September, 0.6 °C lower than that  
362 before the typhoon (Fig. 5c). On 16 September, the SST within AE2 begins to recover, but it starts to  
363 cool again on 18 September due to the influence of Fung-wong.

364 Then we compare the Ro and EKE of AE1 and AE2 before, during and after typhoon. Before being  
365 influenced by the typhoon, the warm eddy AE1 exhibits a more scattered distribution of negative Ro due  
366 to its edge structure, and the EKE values at the eddy boundary are relatively high (Fig. 4d, g). As the  
367 typhoon passes through the eddy, the Ro and EKE of AE1 increase. On 19 September, the average Ro  
368 within AE1 reaches a value of  $-8.2 \times 10^{-2}$ , at the same time, the average EKE increases to its maximum  
369 value of  $325.0 \text{ cm}^2 \text{ s}^{-2}$ . The variation trend of Ro and EKE within the eddy is consistent, increasing from  
370 the passage of the typhoon and starting to recover on 20 September (Fig. 5b-c). This indicates that  
371 although the area of the warm eddy AE1 decreased under the influence of the typhoon, its intensity  
372 increases. On the other hand, for warm eddy AE2, both Ro and EKE decreases after the typhoon passage,  
373 with the Ro decreasing to  $-4.5 \times 10^{-2}$  on 17 September and the EKE decreasing to  $152.0 \text{ cm}^2 \text{ s}^{-2}$  on the 19  
374 September, following by a recovery (Fig. 5f-g). Unlike AE1, AE2 weakens in intensity under the  
375 influence of the typhoon.

376 During the passage of the typhoon, wind stress-driven mixing enhancement and an increase in vertical  
377 shear result a deepening of the MLD, which further strengthens the mixing between the deep cold water  
378 and the upper warm water (Shay and Jaimes, 2009). To avoid a large part of the strong diurnal cycle in  
379 the top few meters of the ocean, 10 m is set as the reference depth (De Boyer Montégut, 2004). A 0.5 °C  
380 threshold difference from 10 m depth is calculated and defined as the MLD (Thompson and Tkalic,  
381 2014). Prior to the influence of typhoon Kalmaegi, the MLD in the AE1 and AE2 regions is deeper (Fig.  
382 4j), with the average MLDs of 32 m and 33 m, respectively. Starting from 14 September, the MLDs are  
383 influenced by typhoon Kalmaegi, with the MLD of AE1 deepening to 37 m and that of AE2 increasing  
384 to 41 m, representing a deepening of 5 m and 8 m, respectively (Fig. 5d, h).

385 Overall, Typhoon Kalmaegi likely exerts distinct impacts on the two warm eddies. Despite both AE1  
386 and AE2 experiencing a decrease in their respective areas by approximately one-third, accompanied by  
387 deepening of the MLD, the amplitude of SLA within AE1 increases by 1.3 cm, whereas AE2 witnesses  
388 a decrease of about 3.1 cm in its amplitude. Furthermore, the SST, Rossby number and EKE within AE1  
389 and AE2 exhibited contrasting patterns.

删除了: relatively

删除了: starts to

删除了:  $\text{cm}^2$

删除了: follows

删除了: weakens

删除了: enhances

删除了: driven by wind stress

删除了: s

设置了格式: 非突出显示

设置了格式: 非突出显示

设置了格式: 非突出显示

设置了格式: 非突出显示

设置了格式: 突出显示

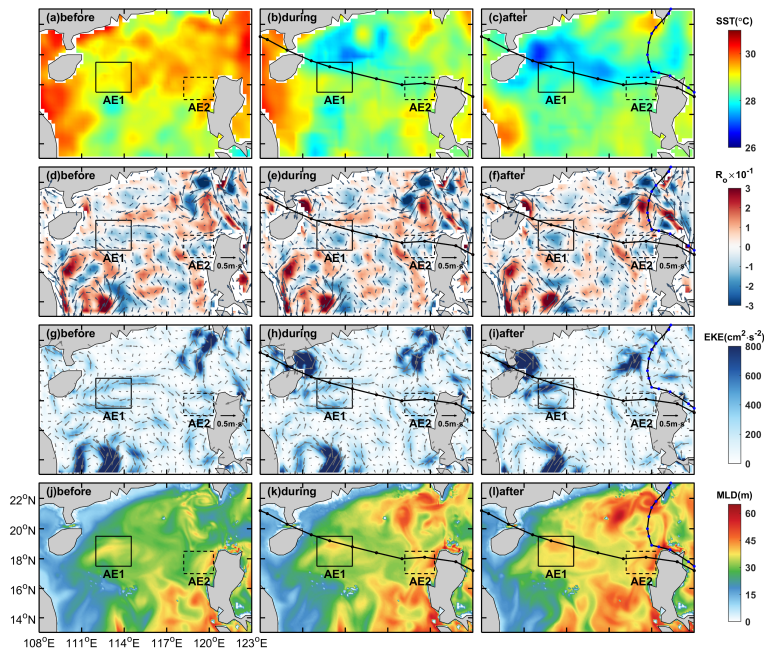
删除了: [RE-WRITE]

删除了: in

删除了: defines

删除了: accompanies

删除了: exhibits



403

404

405

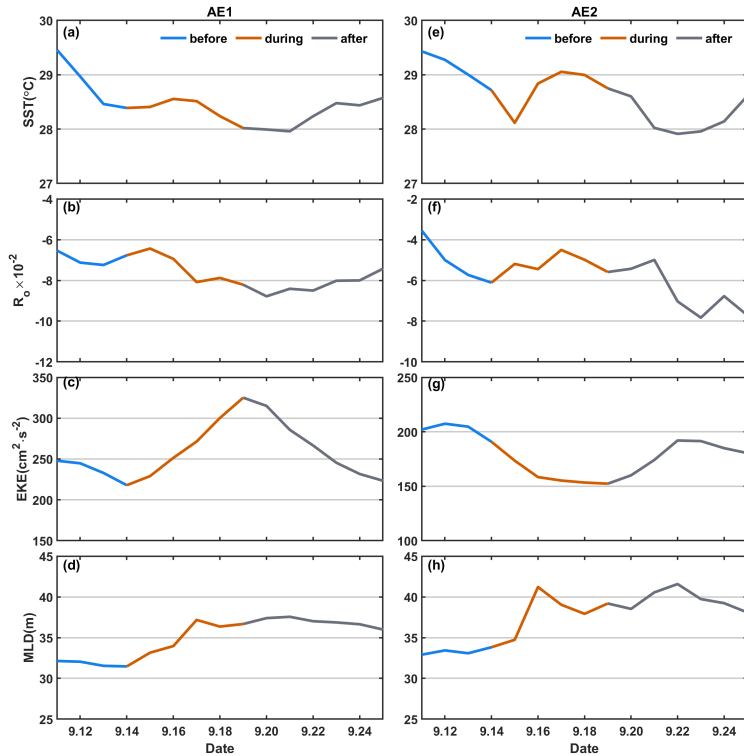
406

407

408

**Figure 4.** The spatial distribution of SST,  $R_e$ , EKE, and MLD before, during and after the passage of TCs. The time periods of 10-13, 15-16 and 19-22 September are designated as stages before, during and after Kalmaegi, respectively. The path of Typhoon Kalmaegi is depicted by a black solid line with black dots, while the path of tropical storm Fung-wong is represented by a black solid line with blue dots in the third column. The solid and dashed boxes correspond to AE1 and AE2, respectively.





409  
 410 **Figure 5.** The time series of sea surface temperature (SST),  $R_\sigma$ , eddy kinetic energy, and mixed layer depth (MLD)  
 411 within the warm eddies' regions (black solid and dashed boxes in Fig. 4). The first column is variables of AE1, the  
 412 second column is for AE2.

413 **3.2 Upper-ocean vertical thermal and salinity structure of eddies**

414 We conducted further analysis on the vertical temperature and salinity structure of the warm eddies  
 415 AE1 and AE2 before and after the Typhoon Kalmaegi using GLORYS12V1 data. During the typhoon's  
 416 passage on 15 September, the temperature above the MLD within AE1 increases by approximately 0.1 °C,  
 417 while the salinity decreases by 0.02psu (Fig. 6). Below the MLD, the temperature shows a significant  
 418 increase, reaching a maximum temperature rise of 1.3 °C. Correspondingly, the salinity below the MLD  
 419 exhibits a decrease of 0.05 psu. Vertical temperature on Kalmaegi's arrival day shows warm pattern from  
 420 surface to 200 m, the salinity shows "fresher-saltier" pattern. These changes lead to a deepening of  
 421 isopycnals by 15 m and a decrease in buoyancy frequency  $N^2$  (Fig. 7a-b), indicating convergence and  
 422 downwelling within the centre of the warm eddy AE1. The near-inertial waves propagates downward  
 423 from surface to 200m during this period (Zhang et al, 2017). The transfer of energy from anticyclonic  
 424 eddy to near-inertial waves is the main reason for the downward propagation and longtime persistence  
 425 of near-inertial energy (Chen et al, 2023).

删除了: conductes

删除了: the isodensity

删除了: [?]

删除了: from

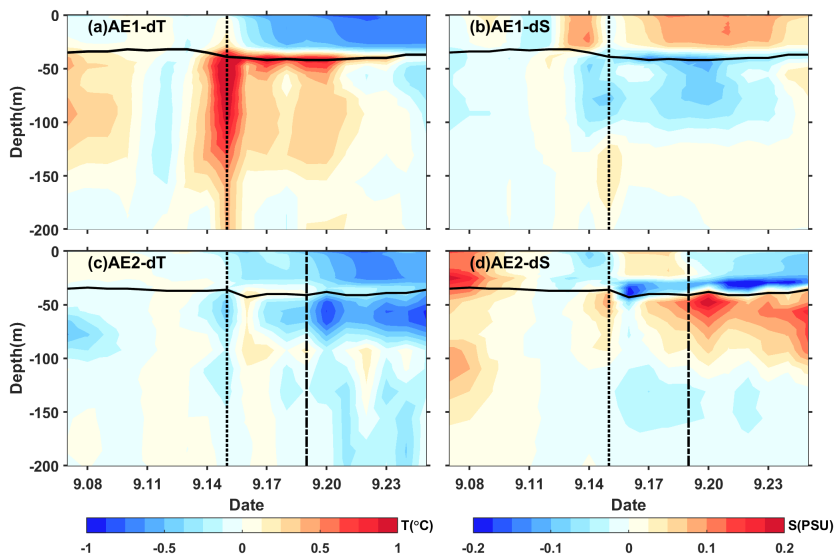
删除了: proppagation

431 After 15 September, the temperature above the MLD decreases, and the salinity shows an increase  
 432 (Fig. 6a-b), resulting in the uplift of the 1021  $\text{kg m}^{-3}$  isopycnal to the sea surface (Fig. 7a-b). The  
 433 subsurface warming and salinity reduction gradually weakens after the Typhoon Kalmaegi but persists  
 434 for about a week after the typhoon's passage until 22 September. During this period, vertical temperature  
 435 pattern becomes "cool-warm" at the center of AE1, and the salinity distribution pattern becomes "saltier-  
 436 fresher-saltier". This persistence can be attributed to the intensified stratification around the MLD, with  
 437  $N^2$  around  $9.0 \times 10^{-4} \text{s}^{-2}$  (Fig. 7b). The increased stability inhibits vertical mixing, restrains the exchange  
 438 of heat and salinity, and leads to smoother density gradients above the MLD (Fig. 7a).

439 The vertical temperature and salinity structure of AE2 exhibits an opposite trend. During the typhoon  
 440 passage on 15 September, AE2 also experiences a cooling trend of  $0.2 \text{ }^\circ\text{C}$ , with a decrease in salinity of  
 441  $0.04 \text{ psu}$  above the MLD. Below the MLD, the temperature shows a consistent decrease, with a change  
 442 of less than  $0.5 \text{ }^\circ\text{C}$  within the subsurface. Correspondingly, the salinity exhibits an increase of  
 443 approximately  $0.08 \text{ psu}$  (Fig. 6c-d). The slightly upward shift of the isopycnals (Fig. 7c) suggests the  
 444 possibility of cold-water upwelling induced by the suction effect of the typhoon. The temperature  
 445 decreases and salinity increases below the MLD are primarily driven by upwelling.

446 Furthermore, when the tropical storm Fung-wong passes through AE2 on 19 September (dashed line  
 447 in Fig. 6c-d), the decreasing trend of subsurface temperature becomes more pronounced, and the  
 448 subsurface salinity exhibits a significant increase. AE2 is more significantly influenced by tropical storm  
 449 Fung-wong. It presents stable stratification with  $N^2$  around  $8.4 \times 10^{-4} \text{s}^{-2}$  at a depth of 42 m, creating a  
 450 barrier layer that prevents the intrusion of high-salinity cold water from the lower layers into the mixed  
 451 layer (Yan et al., 2017).

452



453

删除了: kg

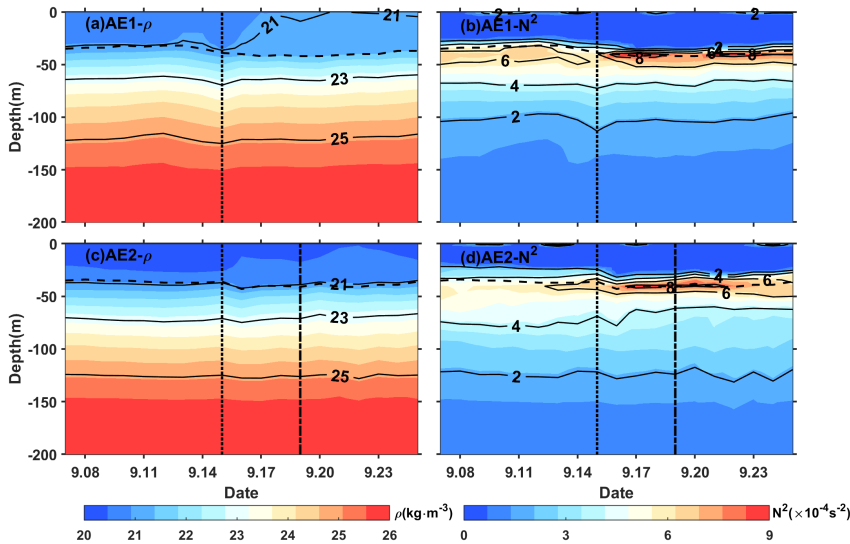
删除了: isodensity

删除了: isodensity

删除了:

删除了: processes

459 **Figure 6.** The timeseries of vertical temperature and salinity anomalies in the center of AE1(a,b) and AE2 (c,d).  
 460 The anomalies were calculated relative to the average value of 10-13 September. The vertical black dotted line  
 461 indicates the Typhoon Kalmaegi's passage, while the vertical black dashed line represents the passage of tropical  
 462 storm Fung-wong. The black solid line is the MLD.



463  
 464 **Figure 7.** Same as Fig. 7, but for density and buoyancy frequency ( $N^2$ ).

### 465 3.3 Comparison of the response between eddies and non-eddies areas

466 To investigate the contrasting response of warm eddies and the non-eddies background to Typhoon  
 467 Kalmaegi, we conduct a comparative analysis of vertical temperature and salinity profiles in these two  
 468 areas. Unfortunately, there is no Argo data around AE1, therefore, we examine data from Argo 2901469,  
 469 which is located within AE2 during the period from 11 to 19 September. The temperature and salinity  
 470 data from Station S5 is considered as the background, with S5 located at a distance of 246 km from  
 471 AE2's center on 15 September (Fig. 1). These profiles are categorized into three periods: pre-typhoon  
 472 (11 September), during-typhoon (15 September), and post-typhoon (19 September).

473 At depths above 40m, both the inside and outside of AE2 experience a decrease in temperature, with  
 474 a cooling of less than  $-1.0^{\circ}\text{C}$ . Four days after the typhoon passage (19 September), the cooling persists  
 475 inside and outside the eddy, with the cooling being more pronounced outside AE2, showing a decrease  
 476 of  $1.2^{\circ}\text{C}$  (Fig. 8c). The salinity within AE2 initially increases by 0.15 psu from the pre-typhoon stage to  
 477 the during-typhoon stage and then decreases by 0.09 psu after the typhoon passage (Fig. 8d). While the  
 478 salinity at Station 5 shows a similar pattern in pre-typhoon and during-typhoon stage, it increases by 0.05  
 479 psu after the typhoon. Two possible processes can explain the difference in salinity trends inside and  
 480 outside AE2. First, during the pre-typhoon to typhoon stage, the entrainment within AE2 may have  
 481 brought the subsurface water, which is saltier, up to the surface, resulting in an increase in salinity. The

删除了: t

删除了: typhoon

删除了: locates

删除了:

删除了: experiences

删除了:

488 second process is related to the typhoon-induced precipitation after the typhoon passage, which lead to a  
489 decrease in salinity. Strong stratification has contributed to the persistence of saltier subsurface water.  
490 While at S5, the increase in salinity is relatively minor.  
491 On 15 September, the subsurface layer at 45 m to 100 m is affected by the cold upwelling, which is  
492 caused by the typhoon, resulting in a cooling and increased salinity within AE2. As the forcing of  
493 Typhoon Kalmaegi diminishes, the upper layer of seawater begins to mix, and warm surface water is  
494 transported to the subsurface layer. Four days later, a warming phenomenon occurs, with the maximum  
495 warm anomaly of 1.2 °C observed at a depth of 75 m (Fig. 8a). The mixing effect outside the eddy is not  
496 significant, resulting in a slight subsurface warming of approximately 0.2 °C, with no significant changes  
497 in salinity. However, on 19 September, a maximum cold anomaly of -1.2°C is observed at depth of 60  
498 m, corresponding to the maximum salinity anomaly of 0.13 psu (Fig. 8c-d). Below 100 m, AE2  
499 experiences a temperature increase of 0.5 °C and a slight decrease in salinity of 0.04 psu. On 19  
500 September, the temperature and salinity within AE2 show little change. However, outside the eddy, a  
501 different response is observed. On 19 September, a cooling trend is observed throughout the water  
502 column, within a range of 0.2 °C, accompanied by a noticeable increase in salinity (Fig. 8c, d), within a  
503 range of 0.06 psu. This indicates that the typhoon causes a significant upwelling outside the eddy region.

删除了: have

删除了:

删除了: only increased slightly

删除了: influences by the downward flow of the eddy itself,

删除了: observes

删除了:

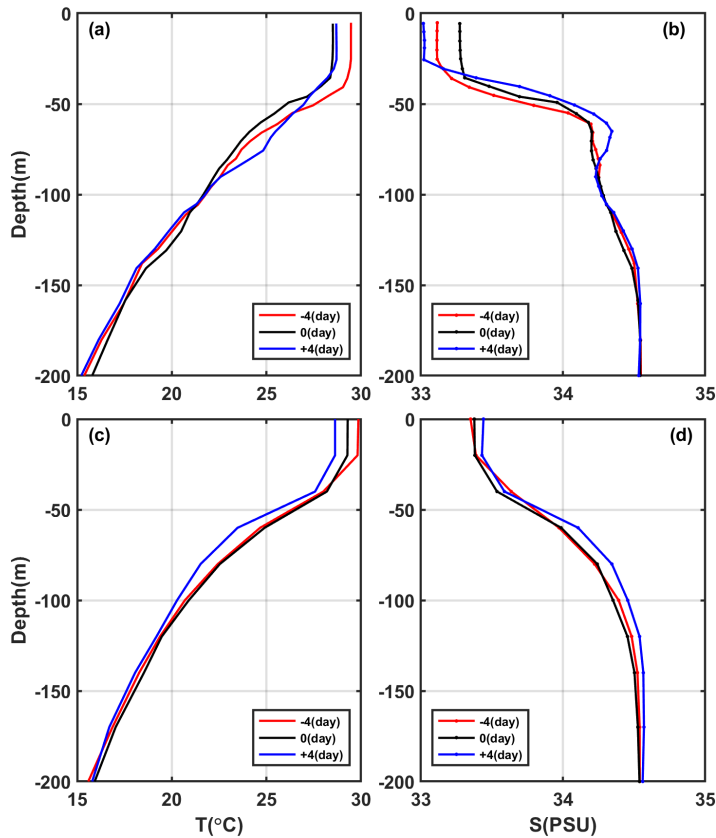
删除了: a

删除了: shows

删除了:

删除了: accompanies

删除了:



515  
 516 **Figure 8.** (a-b) the vertical profile of temperature and salt inside the eddy (Argo 2901469), (c-d) the vertical profiles  
 517 of temperature and salt outside the eddy (S5). The red, black and blue lines represent pre-typhoon, during-typhoon  
 518 and post-typhoon stages.

519 Based on Argo profiles and S5 data, the upper ocean above 200 m inside and outside AE2 responds  
 520 differently to the forcing of the typhoon. In the upper layer (0-40 m), cooling is observed both inside and  
 521 outside the eddy, and it lasts longer. In the subsurface layer (45-100m), after the passage of the typhoon  
 522 (19 September), there is a strong cooling outside the eddy, while warming occurs within AE2. Zhang  
 523 (2022) points out that the sea temperature anomalies mainly depend on the combined effects of mixing  
 524 and vertical advection (cold suction). Mixing causes surface cooling and subsurface warming, while  
 525 upwelling (downwelling) leads to cooling (warming) of the entire upper ocean. The temperature anomaly  
 526 in the subsurface layer depends on the relative strength of mixing and vertical advection, with cold  
 527 anomalies dominating when upwelling is strong, and downwelling amplifying the warming anomalies  
 528 caused by mixing. Therefore, due to the strong influence of upwelling outside the eddy, the temperature  
 529 profile of the entire water column shifts upwards, resulting in cooling of the entire upper ocean. On the  
 530 other hand, influenced by the downwelling associated with the warm eddy itself, a warming anomaly of

删除了: for a

删除了: duration

删除了: influences

删除了:

删除了: associates

删除了:

537 1.2 °C is observed in the subsurface layer. Compared to region AE2, the cold suction effect caused by  
538 the Typhoon Kalmaegi is still evident in the non-eddy area.

539 In the following sections, we delve into the underlying reasons behind these different responses of  
540 AE1 and AE2 to Typhoon Kalmaegi.

#### 541 4. Discussion

542 The EPV is very small before the typhoon, measuring less than  $0.5 \times 10^{-5} \text{ m}_s^{-1}$  in both AE1 and AE2.  
543 However, during 15-16 September (Fig. 9c-f), when typhoon crosses the NSCS, the EPV undergoes  
544 significant changes. Its absolute value increases to over  $1.5 \times 10^{-4} \text{ m}_s^{-1}$  within both AE1 and AE2. AE1  
545 consistently exhibits a predominantly negative EPV during most of this period. Consequently, during  
546 Typhoon Kalmaegi, the negative EPV facilitates downwelling and convergence (Jaimes and Shay, 2015),  
547 leading to a warmer and fresher subsurface layer in AE1 (Fig. 6 a-b).

548 On the other hand, AE2 displays a more fluctuating pattern. It is positive on 14 September, shows  
549 both positive and negative values at 0000 UTC on 15 September, and remains mainly negative from 15  
550 to 16 September, and eventually returning to positive, reflecting a continuously fluctuating process. The  
551 positive EPV in AE2 contributes to the influx of colder subsurface water into the upper layers, resulting  
552 in surface and subsurface water cooling and an increase in salinity in the subsurface (Fig. 6c-d).  
553 Correspondingly, the variations in Ekman layer depth ( $D_E$ ) with the typhoon's passage are similar to EPV,  
554 as shown in Fig. 10. When Kalmaegi approaches at 0000 UTC on 14 September, the mean  $D_E$  within  
555 AE1 is only 21 m, while in AE2, it is 114 m. This indicates that AE2 has already been influenced by  
556 Typhoon Kalmaegi. Subsequently, the depth of the  $D_E$  within AE2 sharply deepens, reaching its  
557 maximum depth of 241 m at 0000 UTC on 15 September, coinciding with the proximity of Typhoon  
558 Kalmaegi's center to AE2. As Kalmaegi moves northwest, the  $D_E$  within AE1 achieves its maximum  
559 depth of 262 m at 0000 UTC on 16 September. The trends of  $D_E$  within AE1 and AE2 are nearly  
560 consistent, but AE1 lags behind AE2 by one day. Starting from 15 September,  $D_E$  within both AE1 and  
561 AE2 gradually shallows, reaching a minimum  $D_E$  of 60 m. This value is 28 m higher than before the  
562 typhoon, indicating the lingering effects of the typhoon through wind. For AE2,  $D_E$  reached its minimum  
563 of 45 m at 0000 UTC on 18 September, later gradually increasing under the influence of tropical storm  
564 Fung-wong.

删除了: Compares

删除了:

删除了: causes

删除了:

删除了: ↩

删除了: .

设置了格式: 上标, 非突出显示

删除了: .

删除了: The EPV of

设置了格式: 上标, 非突出显示

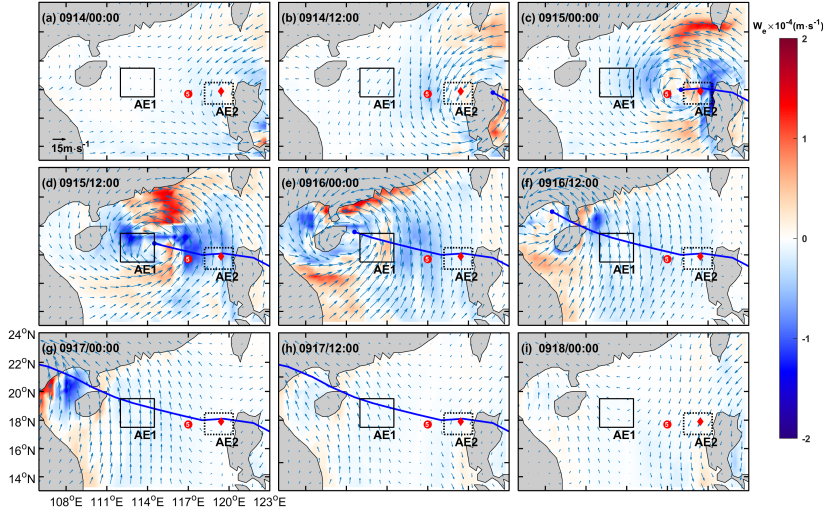
删除了: is

删除了: the time

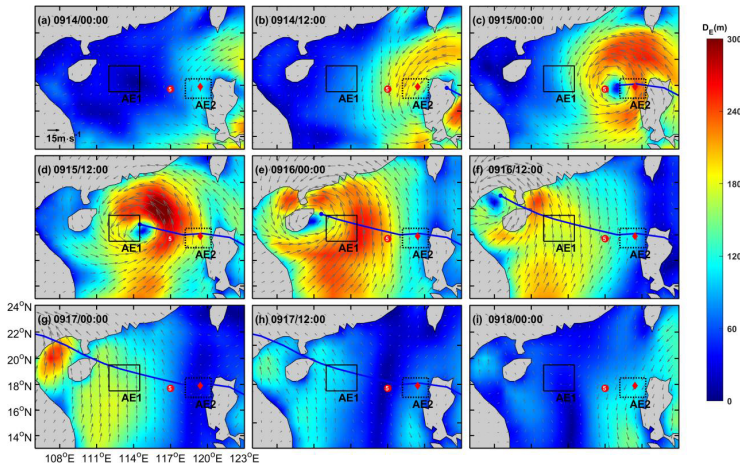
删除了: typhoon

删除了: On the other hand, AE2 exhibits a more fluctuating pattern.

It is positive on 14 September, has both positive and negative values at 0000 UTC on 15 September, and is mainly negative from 15 September to 16 September, and then becomes positive again, which is a constantly fluctuating process. The positive EPV in AE2 contributes to the influx of colder subsurface water into the upper layers, resulting in surface and subsurface water cooling and increases salinity in the subsurface (Fig. 6c-d). Correspondingly, the variations in Ekman layer depth ( $D_E$ ) with the typhoon's passage are similar to EPV, as shown in Fig. 10. When Kalmaegi approaches at 0000 UTC on 14 September, the mean  $D_E$  within AE1 is only 21 m, while in AE2, it is 114 m. This indicates that AE2 has already been influenced by typhoon Kalmaegi. Subsequently, the depth of the  $D_E$  within AE2 sharply deepens, reaching its maximum depth of 241 m at 0000 UTC on 15 September, coinciding with the proximity of typhoon Kalmaegi's center to AE2.



592  
 593 **Figure 9.** Ekman Pumping Velocity (EPV) from 14 September to 18 September (a-i). The color represents the EPV,  
 594 the blue solid line is the path of Kalmaegi, the red dot and diamond are the positions of Station 5 and Argo 2901469  
 595 on 15 September, respectively.

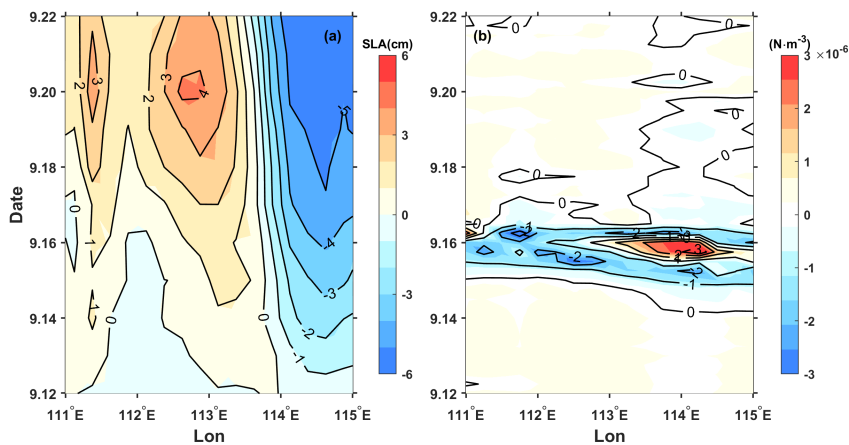


596  
 597 **Figure 10.** Ekman layer depth ( $D_E$ ) from 14 September to 18 September (a-i). The color represents the  $D_E$ , the blue  
 598 solid line is the path of Kalmaegi, the red dot and diamond are the positions of Station 5 and Argo 2901469 on 15  
 599 September, respectively.

600 [After traversing the warm ocean characteristics of AE2, Typhoon Kalmaegi strengthens, resulting in](#)  
 601 [a reduction of the maximum wind radius. As it passed through AE1, the maximum wind radius is 35 km.](#)  
 602 [Notably, the center of AE1 is located outside the typhoon's two-times maximum wind radius,](#)  
 603 [approximately 104 km away from the typhoon center \(Fig. 3\). As mentioned earlier, strong upwelling](#)  
 604 [occurs within two-times maximum wind radius, while weak subsidence exists in the vast area outside](#)



605 [the upwelling region](#) (Jaimes and Shay, 2015). [Hence, the hypothesis presented here suggests that the](#)  
 606 [observed intensification of AE1 on the left side of the typhoon track is more likely attributed to the](#)  
 607 [negative wind stress generated outside the maximum wind radius, driving the enhancement of](#)  
 608 [downwelling in the pre-existing anticyclonic feature in the ocean](#). Starting from 15 September, a  
 609 significant positive sea level anomaly (SLA) to the west of 113.5°E becomes evident, intensifying and  
 610 reaching its maximum on 20 September (Fig. 11a). This strengthening aligns with the increase in the  
 611 amplitude of the warm core of the eddy AE1. A comparison with the wind stress curl anomaly (Fig. 11b)  
 612 reveals that between 15 to 16 September, as the Typhoon Kalmaegi moves over the section at 18.2°N,  
 613 specifically to the west of 113.5°E, it exhibits strong negative wind stress curl anomalies, with a  
 614 maximum intensity of  $-3 \times 10^{-6} \text{ N}\cdot\text{m}^{-3}$ . The negative wind stress curl [induced](#) by the typhoon results in  
 615 favourable surface ocean currents that further [enhances](#) the clockwise rotation of the warm eddy. The  
 616 negative wind stress curl anomaly results [in](#) strong downwelling currents, inputting negative vorticity  
 617 into AE1, leading to its intensification (Fig. 4b-c), as [indicated](#) by the enhanced positive SLA (Fig. 11a).  
 618 Conversely, the region to the east of 113.5°E along the section exhibited negative SLA anomalies. This  
 619 weakening is consistent with the previous observations of the intensified warm core and decreased eddy  
 620 area.



621  
 622 **Figure 11.** The time/longitude plots of (a) SLA anomaly (cm) and (b) wind stress curl ( $\text{N}\cdot\text{m}^{-3}$ ) anomaly at the central  
 623 section of AE1 (18.2°N). The anomalies were calculated relative to the average value of 10-13 September.

624 [The response of AE2 differs from that of AE1 mainly because AE2 is quite near the Typhoon](#)  
 625 [Kalmaegi's track. As the typhoon passes through AE2, the maximum wind radius is 48 km. AE2 is](#)  
 626 [merely 26 km away from the typhoon center](#) (Fig. 3). [The significantly positive wind stress curl at the](#)  
 627 [typhoon center induces upwelling and positive vorticity downward into the eddy](#) (Huang and Wang,  
 628 2022), [and noticeably weakens the eddy, corresponding to the decrease in SLA \(Fig. 12a\)](#). Furthermore,  
 629 [based](#) on the meridional isotherm profiles of the eddy center at three [dates](#), it can be observed that during  
 630 the passage of Typhoon Kalmaegi (15 September), the isotherms in the AE1 region exhibit significant  
 631 subsidence (Fig. 13a), while in the AE2 region, the isotherms show uplift (Fig. 13b). This result aligns

删除了: presents

删除了:

删除了: generates

删除了:

删除了: After traversing the warm ocean characteristics of AE2, Typhoon Kalmaegi becomes stronger and the maximum wind radius becomes smaller. As it passes through AE1, the maximum wind radius is measured at 35 km. Notably, the center of AE1 is located outside the maximum wind radius, approximately 104 km away from the typhoon center (Fig. 3). Hence, the hypothesis presents here suggests that the observed intensification of AE1 on the left side of the typhoon track is more likely attributed to the negative wind stress generated outside the maximum wind radius, driving the enhancement of downwelling in the pre-existing anticyclonic feature in the ocean.

删除了: .

删除了: induces

删除了: enhances

删除了: indicates

删除了:

删除了: .

删除了: . essentially falling within two-times the maximum wind radius of the typhoon

删除了: The response of AE2 is different from AE1 mainly because AE2 is quite near the typhoon Kalmaegi's track. When the typhoon passes through AE2, the maximum wind radius is 48km. AE2 is only 26 km away from the center of the typhoon, and its central area is basically within the maximum wind radius of the typhoon (Fig. 3). The significantly positive wind stress curl at the center of the typhoon induces upwelling and positive vorticity downward into the eddy (Huang and Wang, 2022), noticeably weakens the eddy, corresponding to the decrease in SLA (Fig. 12a)

删除了: bases

删除了:

删除了: periods

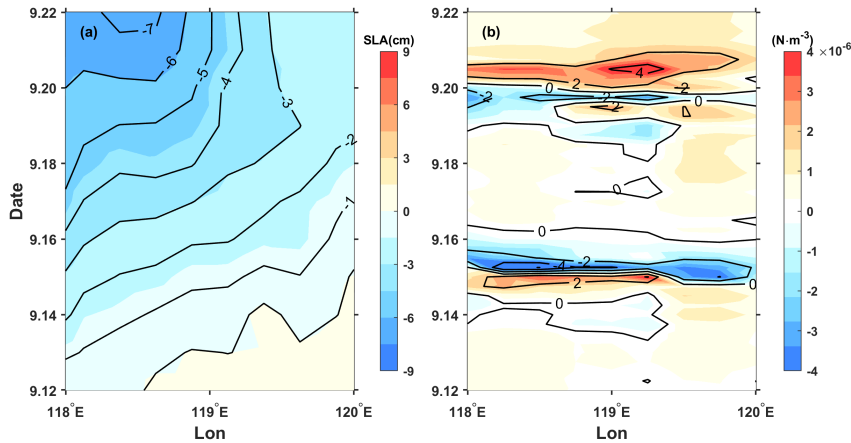
删除了: [?]

设置了格式: 非突出显示



668 with the earlier observation that the convergence and subsidence within the warm eddy AE1 are **enhanced**  
 669 by the influence of the wind stress curl induced by the typhoon, while the intensity of AE2 is weakened.

删除了: enhances



670  
 671 **Figure 12.** Same as Fig.10, but for AE2(17.9 °N).

672 From the above, the relative position of eddies and the typhoon can influence the response of the  
 673 eddies (Lu et al., 2020). The warm eddy AE1, **located** on the left side of the typhoon track, is not  
 674 weakened by the strong cold suction effect **caused** by the typhoon Kalmaegi. Instead, it is strengthened  
 675 due to the stronger negative wind stress curl generated by the typhoon.

删除了: locates

删除了: causes

676 To understand the work done by the Typhoon Kalmaegi on the eddies in the ocean, we estimate the  
 677 total work inputted into the ocean current  $u_c$  using the previously calculated wind stress (Liu et al.,  
 678 2017):

679 
$$W = \int \tau \cdot u_c dt . \quad (10)$$

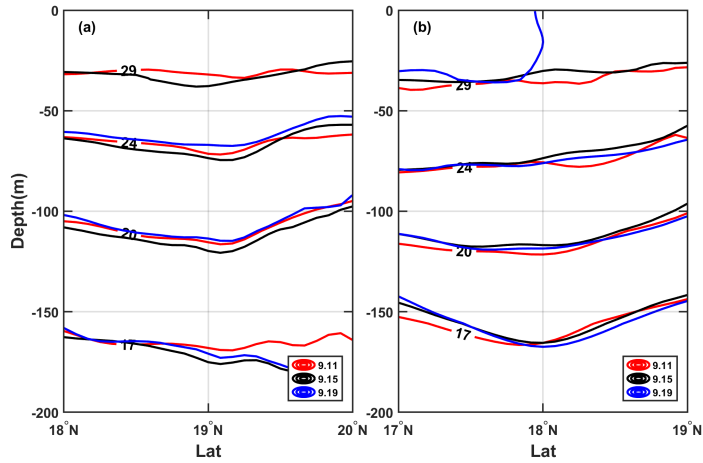
680 Here, we select the region near the typhoon track where the wind speed exceeds  $17 \text{ m}\cdot\text{s}^{-1}$  as the typhoon  
 681 forcing region to **know** the energy input by the typhoon to the warm eddy (Sun et al., 2010). The forcing  
 682 duration over the ocean in the typhoon-affected region and the work done by the typhoon on the surface  
 683 current are shown in Fig. 14. When the angle between the wind and the ocean current is acute, the typhoon  
 684 does positive work on the ocean current. Conversely, when the angle is obtuse, the typhoon does negative  
 685 work on the ocean current. It is evident that the region with the maximum forcing duration by the typhoon  
 686 on AE1 corresponds to the area where the typhoon clearly does positive work on the ocean current,  
 687 accumulating a work done exceeding  $8 \text{ KJ m}^{-2}$ . This acceleration of the flow velocity in the eddy results  
 688 in convergence within the eddy and an increase in SLA, leading to the strengthening of AE1. On the  
 689 other hand, the forcing duration by the typhoon on AE2 is smaller, and the typhoon does negative work  
 690 on the ocean current in most areas, with a cumulative work done within  $-5 \text{ KJ m}^{-2}$ , causing the flow  
 691 velocity within the AE2 to decelerate.

删除了: .

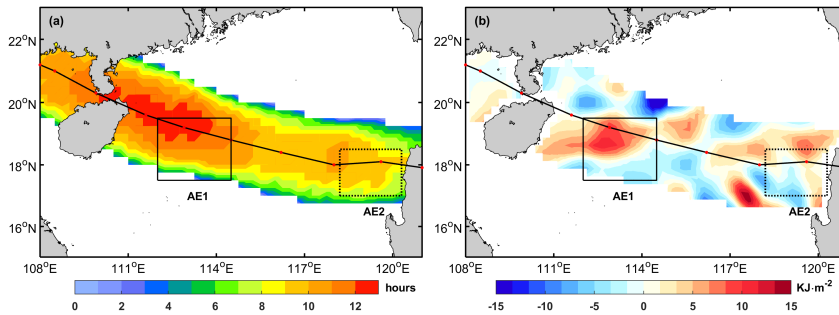
删除了: understand

删除了: [? Use a different word]

删除了: 13



699  
700 **Figure 13.** The meridional isotherm profiles of AE1 (a) and AE2 (b) before (11 September), during (15 September)  
701 and after (19 September) typhoon Kalmaegi.



703  
704 **Figure 14.** (a): the forcing time (unit: hours) of the typhoon; (b): the input work (unit:  $\text{KJ m}^{-2}$ ) of the typhoon to  
705 the current.

706 **5. Summary**

707 Based on multi-satellite observations, in situ measurements, and numerical model data, we have  
708 gained valuable insights into the response of warm eddies AE1 and AE2 in the northern South China Sea  
709 to Typhoon Kalmaegi. Both horizontally and vertically, these eddies display distinct differences.  
710 Horizontally, we observe a reduction of areas by approximately 31% (AE1) and 36% (AE2). AE1,  
711 positions on the left side of the typhoon's track, strengthens with amplitude,  $R_o$  and EKE increasing by  
712 1.3 cm,  $1.4 \times 10^{-2}$  and  $107.2 \text{ cm}^2 \text{ s}^{-2}$  after the typhoon passed. In contrast, AE2, which intersects with the  
713 typhoon's track, weakens with amplitude,  $R_o$  and EKE decreasing by 3.1 cm,  $1.6 \times 10^{-2}$  and  $38.5 \text{ cm}^2 \text{ s}^{-2}$ ,  
714 respectively. Vertically, during the typhoon's passage, AE1 experiences intensified converging  
715 subsidence flow at its center, leading to an increase in temperature and a decrease in salinity above 150  
716 m. This response is more pronounced below the MLD ( $1.3^\circ\text{C}$ ) and persists for about a week after the

删除了: .

删除了: on-site

删除了:  $\text{cm}^2$

删除了:  $\text{cm}^2$

721 typhoon. On the other hand, AE2 exhibits cooling above the MLD, accompanied by a decrease in salinity,  
722 as well as a subsurface temperature drop and salinity increase due to the upwelling of cold water caused  
723 by the typhoon's suction effect. The subsurface cooling and salinity increase in AE2 are further  
724 influenced by Typhoon Fung-wong. Additionally, from the temperature vertical profile of Argo and in-  
725 situ arrays, on 19 September, it can be seen that the non-eddy region also experiences significant cooling,  
726 with a prominent cooling center observed at a depth of 60 m (-1.2 °C). The warm eddy AE2, influenced  
727 by its own downwelling, exhibits enhanced mixing effects, resulting in a subsurface warm anomaly of  
728 1.2 °C.

729 Further analysis reveals that the different responses of the warm eddies can be attributed to factors  
730 such as wind stress curl distribution, which are influenced by the relative position of the warm eddies  
731 and the typhoon track. The wind stress curl induced by the typhoon plays a crucial role in shaping the  
732 response of the warm eddies. AE1, located on the left side of the typhoon's path, experiences prolonged  
733 forcing from the typhoon, resulting in positive work on the ocean current. This inputs a strong negative  
734 wind stress curl into the eddy, enhancing negative EPV and deepening  $D_E$ , so the downwelling within  
735 the AE1 is obvious and contributing to its increased strength. In contrast, AE2, positioned directly below  
736 the typhoon's track, experiences shorter forcing duration and weakens due to the strong positive wind  
737 stress curl at the typhoon's center and shallower  $D_E$ . Furthermore, the absolute value of EPV increases in  
738 both warm eddies during the typhoon's passage, but with differing impacts. The positive EPV contributes  
739 to surface water cooling and the influx of cooler subsurface water, while the negative EPV facilitates  
740 downwelling and intensifies the influence of the warm eddies.

741 While numerous prior studies exploring the interaction between TCs and eddies have predominantly  
742 drawn generalized conclusions, such as the weakening (strengthening) effect of cold (warm) eddies.  
743 Conversely, TCs are recognized for strengthening cold eddies and weakening warm eddies. However,  
744 our study takes a different approach. We aim to illustrate that even when TCs encounter eddies of the  
745 same polarity, the response of these eddies to TCs exhibits variations. This nuanced response is intricately  
746 linked to factors including the relative position of the eddies and the TCs, the eddies' intensity, and the  
747 background current. It is discussed first time in the South China Sea. By analyzing wind stress curl  
748 distribution, EPV, buoyancy frequency and the relative position between the eddies and the typhoon's  
749 track, this case study provides a more nuanced understanding of the mechanisms driving these different  
750 eddy-typhoon interactions in the Northern South China Sea. Moreover, it will further improve the  
751 accuracy of TC forecasts and enhancing the simulation capabilities of air-sea coupled models.

752  
753  
754 *Data availability.* The six-hourly best-track typhoon datasets were accessed on 3 February 2021 by JTWC,  
755 <http://www.usno.navy.mil/JTWC>, JMA, [https://www.jma.go.jp/jma/jma-eng/jma-center/rsmc-hp-pub-](https://www.jma.go.jp/jma/jma-eng/jma-center/rsmc-hp-pub-eg/besttrack.html)  
756 [eg/besttrack.html](http://tcdata.typhoon.gov.cn) and CMA, <http://tcdata.typhoon.gov.cn>. The AVISO product was accessed on 14 February  
757 2021 by <https://marine.copernicus.eu/>. The AVHRR SST data was accessed on 16 March, 2022 by  
758 [ftp://podaac.jpl.nasa.gov/documents/dataset\\_docs/avhrr\\_pathfinder\\_sst.html](ftp://podaac.jpl.nasa.gov/documents/dataset_docs/avhrr_pathfinder_sst.html). The Argo data was accessed  
759 on 4 April, 2022 by <https://dataselection.euro-argo.eu/>. The wind data was accessed on 5 January, 2023 by

删除了: accompanies

删除了: causes

删除了: observes

删除了: influences

删除了: exhibits

删除了: induces

删除了: locates

删除了: positions

带格式的: 缩进: 首行缩进: 1 字符

删除了: In summary, mthe different responses of warm eddies to typhoons provide valuable insights into the complex interactions between the atmosphere and the ocean. Understanding these responses is crucial for accurate climate modeling and weather forecastiBy investigating factors such as wind stress curl distribution, EPV, buoyancy frequency and the relative position of the eddies to the typhoon's track, researchers can gain a more precise understanding of the underlying mechanisms driving these interactions. This knowledge contributes to improved predictions and mitigation strategies for the impacts of typhoons and other extreme weather events, enhances the accuracy of climate models, and advances weather forecasting capabilities.<sup>42</sup>

780 <https://apps.ecmwf.int/datasets/data/interim-full-daily/levtype=sfc/>. The GLORYS12V1 was accessed on  
781 23 March, 2022 by <https://marine.copernicus.eu/>.

782 *Author contributions.* XYL and HZ contributed to the study conception and design. Material preparation, data  
783 collection and analysis were performed by YHH and XYL. GQH and YL contributed to the methodology. The  
784 original manuscript was prepared by XYL and YHH. All the authors contributed to the review and editing of  
785 the manuscript.

786 *Competing interests.* The contact author has declared that none of the authors has any competing interests.

787 *Disclaimer.* Publisher's note: Copernicus Publications remains neutral with regard to jurisdictional claims in  
788 published maps and institutional affiliations.

789 *Acknowledgements.* These data were collected and made freely available by JTWC, JMA, CMA, AVISO, AVHRR,  
790 Argo, ECMWF, COPERNICUS. All figures were created using MATLAB, in particular using the M\_Map toolbox  
791 (Pawlowicz, 2020). The authors thank the anonymous reviewers, whose feedback led to substantial im-  
792 provement of the resulting analyses, figures and manuscript

793 *Financial support.* This research has been supported by the National Natural Science Foundation of China  
794 (42227901), Southern Marine Science and Engineering Guangdong Laboratory (Zhuhai), grant number  
795 SML2020SP007 and SML2021SP207; the Innovation Group Project of Southern Marine Science and  
796 Engineering Guangdong Laboratory (Zhuhai), grant number 311020004 and 311022001; the National  
797 Natural Science Foundation of China, grant number 42206005; the open fund of State Key Laboratory of  
798 Satellite Ocean Environment Dynamics, Second Institute of Oceanography, MNR, grant number QNHX2309;  
799 General scientific research project of Zhejiang Provincial Department of Education, grant number  
800 Y202250609; the Open Foundation from Marine Sciences in the First-Class Subjects of Zhejiang, grant number  
801 OFMS006; State Key Laboratory of Tropical Oceanography (South China Sea Institute of Oceanology Chinese  
802 Academy of Sciences), grant number LTO2220.

803

804

805

## 806 **References**

- 807 Cabanes, C., Grouazel, A., von Schuckmann, K., Hamon, M., Turpin, V., Coatanoan, C., Guinehut, S.,  
808 Boone, C., Ferry, N., and Reverdin, G.: The CORA dataset: validation and diagnostics of ocean  
809 temperature and salinity in situ measurements, *Ocean Sci. Discuss.*, 9, 1273-1312, 2012.
- 810 Chen, G., Hou, Y., and Chu, X.: Mesoscale eddies in the South China Sea: Mean properties,  
811 spatiotemporal variability, and impact on thermohaline structure, *J. Geophys. Res.: Oceans*,  
812 116, <https://doi.org/10.1029/2010jc006716>, 2011.

813 Chen Z, Yu F, Chen Z, et al. Downward Propagation and Trapping of Near-Inertial Waves by a  
814 Westward-moving Anticyclonic Eddy in the Subtropical Northwestern Pacific Ocean[J]. *Journal of*  
815 *Physical Oceanography*, 2023.

816 de Boyer Montégut, C.: Mixed layer depth over the global ocean: An examination of profile data and a  
817 profile-based climatology, *J. Geophys. Res.: Oceans*, 109,<https://doi.org/10.1029/2004jc002378>, 2004.

818 Ezraty, R., Girard-Ardhuin, F., Piollé, J.-F., Kaleschke, L., and Heygster, G.: Arctic and Antarctic sea  
819 ice concentration and Arctic sea ice drift estimated from Special Sensor Microwave data, *Département*  
820 *d’Océanographie Physique et Spatiale, IFREMER, Brest, France and University of Bremen Germany*, 2,  
821 2007.

822 Huang, L., Cao, R., and Zhang, S.: Distribution and Oceanic Dynamic Mechism of Precipitation Induced  
823 by Typhoon Lekima, *American Journal of Climate Change*, 11, 133-  
824 154,<https://doi.org/10.4236/ajcc.2022.112007>, 2022.

825 Huang, X. and Wang, G.: Response of a Mesoscale Dipole Eddy to the Passage of a Tropical Cyclone:  
826 A Case Study Using Satellite Observations and Numerical Modeling, *Remote Sens.*,  
827 14,<https://doi.org/10.3390/rs14122865>, 2022.

828 Jaimes, B. and Shay, L. K.: Enhanced Wind-Driven Downwelling Flow in Warm Oceanic Eddy Features  
829 during the Intensification of Tropical Cyclone Isaac (2012): Observations and Theory, *J. Phys. Oceanogr.*,  
830 45, 1667-1689,<https://doi.org/10.1175/jpo-d-14-0176.1>, 2015.

831 Jullien, S., Menkès, C. E., Marchesiello, P., Jourdain, N. C., Lengaigne, M., Koch-Larrouy, A., Lefèvre,  
832 J., Vincent, E. M., and Faure, V.: Impact of tropical cyclones on the heat budget of the South Pacific  
833 Ocean, *J. Phys. Oceanogr.*, 42, 1882-1906,<https://doi.org/10.1175/JPO-D-11-0133.1>, 2012.

834 Kessler, W. S.: The circulation of the eastern tropical Pacific: A review, *Prog. Oceanogr.*, 69, 181-  
835 217,<https://doi.org/10.1016/j.pocan.2006.03.009>, 2006.

836 Li, Q., Sun, L., Liu, S., Xian, T., and Yan, Y.: A new mononuclear eddy identification method with  
837 simple splitting strategies, *Remote Sens. Lett.*, 5, 65 - 72,<https://doi.org/10.1080/2150704x.2013.872814>,  
838 2014.

839 Li, X., Zhang, X., Fu, D., and Liao, S.: Strengthening effect of super typhoon Rammasun (2014) on  
840 upwelling and cold eddies in the South China Sea, *J. Oceanol. Limnol.*, 39, 403-  
841 419,<https://doi.org/10.1007/s00343-020-9239-x>, 2021.

842 Lin, I. I., Chou, M.-D., and Wu, C.-C.: The Impact of a Warm Ocean Eddy on Typhoon Morakot (2009):  
843 A Preliminary Study from Satellite Observations and Numerical Modelling, *TAO: Terrestrial,*  
844 *Atmospheric and Oceanic Sciences*, 22,[https://doi.org/10.3319/tao.2011.08.19.01\(tm\)](https://doi.org/10.3319/tao.2011.08.19.01(tm)), 2011.

845 Lin, I. I., Wu, C.-C., Emanuel, K. A., Lee, I. H., Wu, C.-R., and Pun, I.-F.: The Interaction of  
846 Supertyphoon Maemi (2003) with a Warm Ocean Eddy, *Mon. Weather Rev.*, 133, 2635-  
847 2649,<https://doi.org/10.1175/MWR3005.1>, 2005.

848 Liu, F. and Tang, S.: Influence of the Interaction Between Typhoons and Oceanic Mesoscale Eddies on  
849 Phytoplankton Blooms, *J. Geophys. Res.: Oceans*, 123, 2785-  
850 2794,<https://doi.org/10.1029/2017jc013225>, 2018.

851 Liu, S.-S., Sun, L., Wu, Q., and Yang, Y.-J.: The responses of cyclonic and anticyclonic eddies to  
852 typhoon forcing: The vertical temperature-salinity structure changes associated with the horizontal  
853 convergence/divergence, *J. Geophys. Res.: Oceans*, 122, 4974-  
854 4989,<https://doi.org/10.1002/2017JC012814>, 2017.

855 Lu, Z., Wang, G., and Shang, X.: Response of a Preexisting Cyclonic Ocean Eddy to a Typhoon, *J. Phys.*  
856 *Oceanogr.*, 46, 2403-2410,<https://doi.org/10.1175/jpo-d-16-0040.1>, 2016.

857 Lu, Z., Wang, G., and Shang, X.: Strength and Spatial Structure of the Perturbation Induced by a Tropical  
858 Cyclone to the Underlying Eddies, *J. Geophys. Res.: Oceans*, 125, <https://doi.org/10.1029/2020jc016097>,  
859 2020.

860 Lu, Z., Wang, G., and Shang, X.: Observable large-scale impacts of tropical cyclones on subtropical gyre,  
861 *J. Phys. Oceanogr.*, <https://doi.org/10.1175/JPO-D-22-0230.1>, 2023.

862 Ma, Z., Zhang, Z., Fei, J., and Wang, H.: Imprints of Tropical Cyclones on Structural Characteristics of  
863 Mesoscale Oceanic Eddies Over the Western North Pacific, *Geophys. Res. Lett.*,  
864 48, <https://doi.org/10.1029/2021gl092601>, 2021.

865 Ma, Z., Fei, J., Liu, L., Huang, X., and Li, Y.: An Investigation of the Influences of Mesoscale Ocean  
866 Eddies on Tropical Cyclone Intensities, *Mon. Weather Rev.*, 145, 1181-  
867 1201, <https://doi.org/10.1175/mwr-d-16-0253.1>, 2017.

868 Ning, J., Xu, Q., Zhang, H., Wang, T., and Fan, K.: Impact of Cyclonic Ocean Eddies on Upper Ocean  
869 Thermodynamic Response to Typhoon Soudelor, *Remote Sens.*, 11, <https://doi.org/10.3390/rs11080938>,  
870 2019.

871 Oey, L. Y., Ezer, T., Wang, D. P., Fan, S. J., and Yin, X. Q.: Loop Current warming by Hurricane Wilma,  
872 *Geophys. Res. Lett.*, 33, <https://doi.org/10.1029/2006gl025873>, 2006.

873 Price, J. F.: Upper Ocean Response to a Hurricane, *J. Phys. Oceanogr.*, [https://doi.org/10.1175/1520-0485\(1981\)011%3C0153:UORTAH%3E2.0.CO;2](https://doi.org/10.1175/1520-0485(1981)011%3C0153:UORTAH%3E2.0.CO;2), 1981.

875 Pujol, M.-I., Faugère, Y., Taburet, G., Dupuy, S., Pelloquin, C., Ablain, M., and Picot, N.: DUACS  
876 DT2014: the new multi-mission altimeter data set reprocessed over 20 years, *Ocean Sci.*, 12, 1067-  
877 1090, <https://doi.org/10.5194/os-12-1067-2016>, 2016.

878 Rudzin, J. E. and Chen, S.: On the dynamics of the eradication of a warm core mesoscale eddy after the  
879 passage of Hurricane Irma (2017), *Dyn. Atmos. Oceans*,  
880 100, <https://doi.org/10.1016/j.dynatmoce.2022.101334>, 2022.

881 Shang, X.-d., Zhu, H.-b., Chen, G.-y., Xu, C., and Yang, Q.: Research on Cold Core Eddy Change and  
882 Phytoplankton Bloom Induced by Typhoons: Case Studies in the South China Sea, *Adv. Meteorol.*, 2015,  
883 1-19, <https://doi.org/10.1155/2015/340432>, 2015.

884 Shay, L. K. and Jaimes, B.: Mixed Layer Cooling in Mesoscale Oceanic Eddies during Hurricanes  
885 Katrina and Rita, *Mon. Weather Rev.*, 137, 4188-4207, <https://doi.org/10.1175/2009mwr2849.1>, 2009.

886 Shay, L. K. and Jaimes, B.: Near-Inertial Wave Wake of Hurricanes Katrina and Rita over Mesoscale  
887 Oceanic Eddies, *J. Phys. Oceanogr.*, 40, 1320-1337, <https://doi.org/10.1175/2010jpo4309.1>, 2010.

888 Shay, L. K., Goni, G. J., and Black, P. G.: Effects of a Warm Oceanic Feature on Hurricane Opal, *Mon.*  
889 *Weather Rev.*, 128, 1366-1383, [https://doi.org/10.1175/1520-0493\(2000\)128<1366:EOAWOF>2.0.CO;2](https://doi.org/10.1175/1520-0493(2000)128<1366:EOAWOF>2.0.CO;2), 2000.

891 Song, D., Guo, L., Duan, Z., and Xiang, L.: Impact of Major Typhoons in 2016 on Sea Surface Features  
892 in the Northwestern Pacific, *Water*, 10, <https://doi.org/10.3390/w10101326>, 2018.

893 Sun, J., Ju, X., Zheng, Q., Wang, G., Li, L., and Xiong, X.: Numerical Study of the Response of Typhoon  
894 Hato (2017) to Grouped Mesoscale Eddies in the Northern South China Sea, *J. Geophys. Res.: Atmos.*,  
895 128, <https://doi.org/10.1029/2022jd037266>, 2023.

896 Sun, L., Yang, Y., Xian, T., Lu, Z., and Fu, Y.: Strong enhancement of chlorophyll a concentration by a  
897 weak typhoon, *Mar. Ecol. Prog. Ser.*, 404, 39-50, <https://doi.org/10.3354/meps08477>, 2010.

898 Sun, L., Li, Y.-X., Yang, Y.-J., Wu, Q., Chen, X.-T., Li, Q.-Y., Li, Y.-B., and Xian, T.: Effects of super  
899 typhoons on cyclonic ocean eddies in the western North Pacific: A satellite data-based evaluation

900 between 2000 and 2008, *J. Geophys. Res.: Oceans*, 119, 5585-  
901 5598,<https://doi.org/10.1002/2013jc009575>, 2014.

902 Thompson, B. and Tkalich, P.: Mixed layer thermodynamics of the Southern South China Sea, *Clim.*  
903 *Dyn.*, 43, 2061-2075,<https://doi.org/10.1007/s00382-013-2030-3>, 2014.

904 Wada, A. and Usui, N.: Impacts of Oceanic Preexisting Conditions on Predictions of Typhoon Hai-Tang  
905 in 2005, *Adv. Meteorol.*, 2010, 756071,<https://doi.org/10.1155/2010/756071>, 2010.

906 Walker, N. D., Leben, R. R., and Balasubramanian, S.: Hurricane-forced upwelling and  
907 chlorophyllaenhancement within cold-core cyclones in the Gulf of Mexico, *Geophys. Res. Lett.*, 32, n/a-  
908 n/a,<https://doi.org/10.1029/2005gl023716>, 2005.

909 Wang, G., Su, J., Ding, Y., and Chen, D.: Tropical cyclone genesis over the south China sea, *J. Mar.*  
910 *Syst.*, 68, 318-326,<https://doi.org/10.1016/j.jmarsys.2006.12.002>, 2007.

911 Wang, G., Zhao, B., Qiao, F., and Zhao, C.: Rapid intensification of Super Typhoon Haiyan: the  
912 important role of a warm-core ocean eddy, *Ocean Dyn.*, 68, 1649-1661,[https://doi.org/10.1007/s10236-](https://doi.org/10.1007/s10236-018-1217-x)  
913 [018-1217-x](https://doi.org/10.1007/s10236-018-1217-x), 2018.

914 Xiu, P., Chai, F., Shi, L., Xue, H., and Chao, Y.: A census of eddy activities in the South China Sea  
915 during 1993–2007, *J. Geophys. Res.: Oceans*, 115,<https://doi.org/10.1029/2009jc005657>, 2010.

916 Yan, Y., Li, L., and Wang, C.: The effects of oceanic barrier layer on the upper ocean response to tropical  
917 cyclones, *J. Geophys. Res.: Oceans*, 122, 4829-4844,<https://doi.org/10.1002/2017jc012694>, 2017.

918 Yu, F., Yang, Q., Chen, G., and Li, Q.: The response of cyclonic eddies to typhoons based on satellite  
919 remote sensing data for 2001–2014 from the South China Sea, *Oceanologia*, 61, 265-  
920 275,<https://doi.org/10.1016/j.oceano.2018.11.005>, 2019.

921 Yu, J., Lin, S., Jiang, Y., and Wang, Y.: Modulation of Typhoon-Induced Sea Surface Cooling by  
922 Preexisting Eddies in the South China Sea, *Water*, 13,<https://doi.org/10.3390/w13050653>, 2021.

923 Zhang, H.: Modulation of Upper Ocean Vertical Temperature Structure and Heat Content by a Fast-  
924 Moving Tropical Cyclone, *J. Phys. Oceanogr.*, 53, 493-508,<https://doi.org/10.1175/jpo-d-22-0132.1>,  
925 2022.

926 Zhang, H., Chen, D., Zhou, L., Liu, X., Ding, T., and Zhou, B.: Upper ocean response to typhoon  
927 Kalmaegi (2014), *J. Geophys. Res.: Oceans*, 121, 6520-6535,<https://doi.org/10.1002/2016jc012064>,  
928 2016.

929 Zhang, Y., Zhang, Z., Chen, D., Qiu, B., and Wang, W.: Strengthening of the Kuroshio current by  
930 intensifying tropical cyclones, *Science*, 368, 988-993,<https://doi.org/10.1126/science.aax5758>, 2020.

931